

Stability of line-node semimetals with strong Coulomb interactions and properties of the symmetry-broken state

Carlos Naya , Tommaso Bertolini, and Johan Carlström 

Department of Physics, Stockholm University, 106 91 Stockholm, Sweden

 (Received 8 March 2022; revised 30 November 2022; accepted 20 December 2022; published 31 January 2023)

We study the stability and phenomenology of line-node semimetals in the presence of Coulomb interactions. Our results indicate a phase transition to a chiral insulating state that occurs at a finite interaction threshold, which we determine. We also compute the Landau levels for out-of-plane and in-plane magnetic fields in the symmetric and symmetry-broken phases. We find that the magnetic field couples to the chiral order parameter, implying that this degree of freedom can be manipulated *in situ* in experiments. Finally, we check the existence of edge states in the symmetry-broken phase. On the system's boundary, we note that the metallic “drum-head” states that exist in the symmetric phase are gapped out. However, the symmetry-broken phase permits topological defects in the macroscopic order parameter in the form of domain walls, which host metallic “interface states.” These consist of linelike gap-closings that occur on the two-dimensional interfaces.

DOI: [10.1103/PhysRevResearch.5.013069](https://doi.org/10.1103/PhysRevResearch.5.013069)

Topological semimetals exhibit a band structure that is gapped everywhere except at a few nodal points, where the bands meet. The topological nature of these protects them against perturbations and also gives rise to unique phenomena such as the chiral anomaly—where nodal points act as sources and sinks of a spontaneous current—and Fermi arcs, which are direct manifestations of the bulk topology [1]. Applications of topological semimetals are thus far mainly as building blocks of information technology [2–4]. Several of these materials exhibit a large magnetoresistance effect [5] that may be exploited in magnetic field sensors [6] and spintronic devices [7].

In the search for new and technologically useful semimetals, symmetry-protected topological phases have emerged as an important platform that dramatically expands the types of nodal features realized in a material. Typically, this involves a combination of point group symmetries and explicitly broken time-reversal or inversion symmetry. The result is a wide class of band touching points that carry more than unit topological charge [8,9] and may also involve multiple bands [10,11] or have to be classified as line-nodes [12–18].

While the explicit reliance on symmetry significantly widens the scope of topological and semimetallic materials, it also has implications for the role of correlations in these: In tight-binding models of bilayer graphene, the dispersion is quadratic around the nodal points, yet the system develops a nematic instability at an infinitesimal interaction [19]. For multiple-charge Weyl nodes and line-node semimetals with

contact interaction, renormalization-group theory indicates instabilities at a finite threshold [20,21]. This is also true for single-layer graphene, where actual material parameters are situated close to a chiral symmetry-breaking regime [22]. Thus, semimetallic phases that depend explicitly on symmetry may be susceptible to correlation effects that destroy the underlying symmetry. This is both an obstacle and an opportunity, as symmetry-breaking may give rise to topological phases and phenomena that have no equivalent in noninteracting systems.

Reliably predicting the parameter regimes where symmetry-protected topological phases remain stable faces several delicate problems. The absence of screening means that interactions are effectively long-ranged, leading to infrared divergencies. Furthermore, competition between correlation effects originating from different lengthscales is plausible. For example, in graphene, the long-range part of the interaction drives the system towards an asymptotically free Dirac liquid with divergent Fermi velocity as $T \rightarrow 0$, without causing any instabilities [23]. Thus, the renormalization of the dispersion occurring primarily at the infrared end increases the effective kinetic energy relative to the short-range part of the interaction, which is believed to drive the phase transition. Therefore, an accurate solution to this class of problems requires that all lengthscales are treated on an equal footing.

A type of symmetry-protected topological phase that has attracted considerable interest is the nodal-line semimetal. Predictions of this state have been made in TiTaSe_2 [15], CaAgP [16], Ca_3P_2 [17], and ZrSiS [24] based on reflection symmetry. In PbTaSe_2 it has also been confirmed by angle-resolved photoemission spectroscopy [14]. Recently, the observations of strongly renormalized transport properties and Fermi velocity—as compared to density functional theory (DFT) calculations—in ZrSiS were interpreted as an indication of a strongly correlated line-node semimetal [25].

Published by the American Physical Society under the terms of the Creative Commons Attribution 4.0 International license. Further distribution of this work must maintain attribution to the author(s) and the published article's title, journal citation, and DOI.

In this work, we address the stability of line-node semimetals as well as the phenomenology of the symmetry-broken phase. In the first section, we use diagrammatic simulation techniques [26] to establish quantitative criteria for the stability of line-node semimetals in the presence of long-range interactions. Our results indicate an instability occurring at a finite interaction threshold that gives rise to a chiral insulator. In the second part, we explore the phenomenology of the chiral phase. We find that topological defects in the macroscopic order host metallic “interface states” in the otherwise insulating system. We also show that the chiral order couples to an external magnetic field, providing a means to control it *in situ*.

I. STABILITY OF LINE-NODE SEMIMETALS

We consider the case of a single nodal line with a bare Fermi velocity of v_f^0 running along the z -axis,

$$H_0(\mathbf{k}) = v_f^0 \mathbf{k}_{xy} \cdot \boldsymbol{\sigma}, \quad \mathbf{k}_{xy} = \{k_x, k_y\}, \quad (1)$$

with an interaction of the form

$$V(\mathbf{k}) = \frac{\alpha}{\mathbf{k}^2 + \lambda^{-2}}. \quad (2)$$

Here, λ is a fictitious screening length introduced to regularize the series, and we are thus principally interested in the limit $\lambda \rightarrow \infty$. We consider a cylindrical domain given by

$$|\mathbf{k}_z| \leq \Lambda, \quad \sqrt{\mathbf{k}_x^2 + \mathbf{k}_y^2} \leq \Lambda, \quad (3)$$

where Λ is the ultraviolet cutoff. Because of a scale invariance associated with the linear dispersion, the only relevant lengthscale in the low-temperature limit is the ratio of the UV cutoff and the inverse screening length Λ/λ^{-1} . To see this, we may choose a temperature and energy scale where the temperature is unity by rewriting the partition function $z(\beta, H) = z(1, \beta H)$. This gives a bare Green’s function,

$$\frac{1}{i\omega - \beta H_0(\mathbf{k})} = G_0(\omega, \beta \mathbf{k}), \quad \omega = (2n + 1)\pi, \quad (4)$$

where we have exploited the linearity of H_0 in \mathbf{k} . Diagrammatic corrections to the Green’s function take the form

$$\delta G(\omega, \beta \mathbf{k}) = \prod_{i=1}^N d\mathbf{k}_i \prod_{j=1}^N \beta V(\mathbf{k}_j) \prod_{l=1}^{2N+1} G_0(\omega_l, \beta \mathbf{k}_l), \quad (5)$$

where N is the expansion order. Here, the momenta $\{\mathbf{k}_j\}$ depend on $\{\mathbf{k}_i\}$ and the external momentum \mathbf{k} in a way that is determined by the diagram topology. If we introduce a change of scale $\mathbf{k}' = \beta \mathbf{k}$, we obtain

$$\delta G(\omega, \mathbf{k}') = \prod_{i=1}^N \frac{d\mathbf{k}'_i}{\beta^D} \prod_{j=1}^N \beta V\left[\frac{\mathbf{k}'_j}{\beta}\right] \prod_{l=1}^{2N+1} G_0(\omega_l, \mathbf{k}'_l). \quad (6)$$

For a screened Coulomb interaction in $D = 3$, we find

$$\beta^{-D} \beta \frac{\alpha}{\mathbf{k}'^2/\beta^2 + \lambda^{-2}} = \frac{\alpha}{\mathbf{k}'^2 + \beta^2 \lambda^{-2}}. \quad (7)$$

The UV cutoff changes scale as $\Lambda \rightarrow \beta \Lambda$, giving

$$G(\omega, \beta, \mathbf{k}, \lambda^{-1}, \Lambda) = G(\omega, 1, \mathbf{k}', \beta \lambda^{-1}, \beta \Lambda), \quad (8)$$

which is characterized by the ratio Λ/λ^{-1} in the limit $\beta \rightarrow \infty$.

In the perturbative regime, the nodal line (1) is protected by a symmetry due to being odd under an orthonormal map $\mathbf{k} \rightarrow -\mathbf{k}$. The implication of this symmetry is that on the k_z -axis, the Green’s function must have a pole at zero energy as long as the series expansion remains convergent [27]. Correspondingly, destroying the semimetallic phase requires breaking this symmetry. In a diagrammatic framework, this phase transition can be identified via a divergent susceptibility with respect to a symmetry-breaking perturbation.

A. Contact interaction

The simplest case for the model (1) and (2) occurs when taking $\alpha \rightarrow \alpha \lambda^{-2}$ and $\lambda \rightarrow 0$, which corresponds to contact interaction. In this scenario, self-consistent Fock theory can be conducted analytically, and it provides a simple illustration of the instability. Specifically, the self-energy satisfies the relation

$$\Sigma(\omega_m, \mathbf{k}) = \frac{1}{\beta} \sum_n \int \frac{d^3 q}{(2\pi)^3} \frac{\alpha}{G_0^{-1}(\omega'_n, \mathbf{q}) - \Sigma(\omega'_n, \mathbf{q})}. \quad (9)$$

Here, it should be noted that at the level of Fock theory, Σ is independent of frequency, and thus *de facto* takes the form of a correction to the effective dispersion. Furthermore, contact interaction does not renormalize the Fermi velocity since $H_0(\mathbf{k})$ is an odd function. Since the self-energy is translation-invariant, it must therefore take the form $\Sigma(\mathbf{k}) = \Delta \sigma_z$. Inserting this self-energy in (9) and summing over frequency, we obtain

$$\Sigma(\mathbf{k}) = \Delta \sigma_z = \int \frac{d^3 q}{(2\pi)^3} \alpha \frac{H_0(\mathbf{q}) + \Sigma(\mathbf{q})}{2\sqrt{(v_f^0 q_{xy})^2 + \Delta^2}} \times \tanh \frac{\beta \sqrt{(v_f^0 q_{xy})^2 + \Delta^2}}{2}, \quad (10)$$

where the integral of H_0 over \mathbf{k} vanishes. Thus, Eq. (10) provides a self-consistent equation for Δ as a function of the coupling strength, whose solutions will provide the gap parameter in this regime. Solutions for which Δ is finite correspond to a symmetry-broken state, while the symmetric phase is characterized by a vanishing gap. In the low-temperature limit, and for a cylindrical domain (3) with $\Lambda = 1$, the integral (10) provides an algebraic expression for the gap of the form

$$\frac{\eta}{2v_f^0} \left(\sqrt{1 + \frac{\Delta^2}{(v_f^0)^2}} - \left| \frac{\Delta}{v_f^0} \right| \right) - 1 = 0, \quad (11)$$

where we have introduced $\eta = \alpha(2\pi)^{-2}$. Equation (11) predicts a critical coupling strength $\eta_c/v_f^0 = 2$; see Fig. 1. Above this threshold, the gap is given by

$$\frac{\Delta}{v_f^0} = \frac{\eta}{4v_f^0} - \frac{v_f^0}{\eta}. \quad (12)$$

The onset of a chiral phase at a finite interaction strength is consistent with results from renormalization-group theory for contact interaction [21], and it can be directly traced from

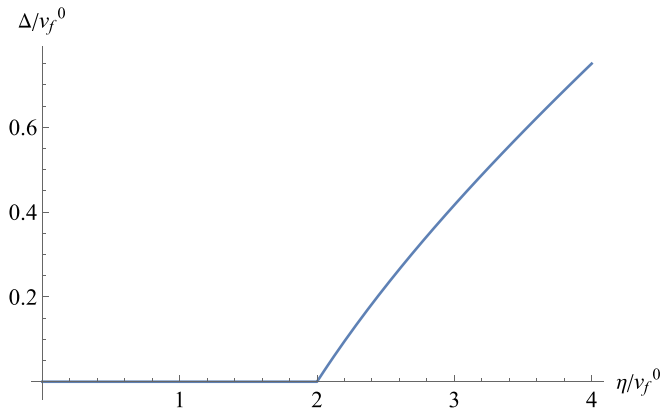


FIG. 1. Self-consistent solution for the gap with contact interactions, as a function of the rescaled coupling strength η . A second-order transition is established at $\eta_c/v_f^0 = 2$.

Eq. (10): For small values of Δ , the self-consistency equation scales as $\Delta \sim \Delta\alpha/v_f^0$, indicating an instability at a finite threshold of α/v_f^0 .

B. Simulations

To check the stability of the semimetallic phase for long-range interactions, we compute the diagrammatic expansion via a protocol that is based on the stochastic sampling of Feynman-type graphs. Within this framework, the space of connected diagrams for the self-energy is sampled through a metropolis-type random walk [26,28–30]. We work in imaginary time and compute the self-energy, which we then use to solve Dyson's equation [31]:

$$G(\omega, \mathbf{k}) = \frac{1}{i\omega - H_0(\mathbf{k}) - \Sigma(\omega, \mathbf{k})}. \quad (13)$$

Here, we use a sampling protocol based on the worm algorithm as described in [32]. We employ a bold scheme where the expansion is conducted in dressed Green's functions while retaining only skeleton graphs. Thus, at order $N = 1$, the solution corresponds to self-consistent Fock theory. We do not employ bold interaction lines since this is expected to have little advantage for a semimetallic system.

Following the scaling relation (8), we can without loss of generality set $\Lambda = 1$. This gives a volume of the momentum space of 2π . We then rewrite the integral over \mathbf{k} as

$$\int \frac{d\mathbf{k}}{(2\pi)^D} = \frac{1}{(2\pi)} \int d\mathbf{k} \frac{\eta}{\alpha}, \quad \eta = \alpha(2\pi)^{-2}, \quad (14)$$

which defines a rescaled interaction parameter η and a set of units where the integral over momenta is of measure unity.

We parametrize the temperature and scale in terms of a variable γ so that

$$\Lambda = 1, \quad \eta = 2^\gamma \tilde{\eta}, \quad v_f^0 = 2^\gamma \tilde{v}_f^0, \quad \lambda^{-1} = 2^{-\gamma} \tilde{\lambda}^{-1}. \quad (15)$$

The limit $\gamma \rightarrow \infty$ thus corresponds to zero temperature and a divergent ratio Λ/λ^{-1} . An observable that is convergent in this limit should correspondingly be a function of η/v_f^0 .

To obtain a self-consistent solution for the model (1) and (2), we consider a frequency and momentum-independent

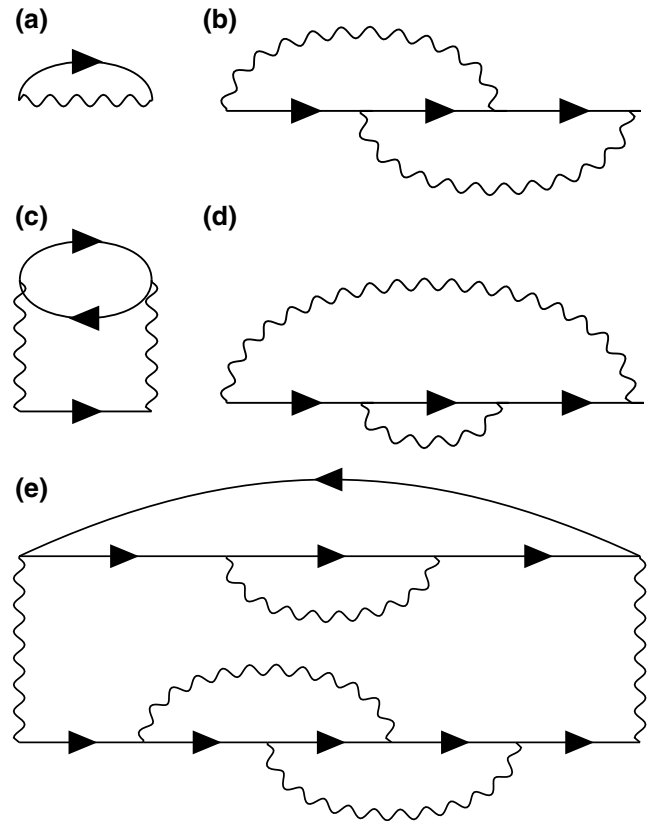


FIG. 2. Diagram topologies for the self-energy: We conduct a summation of the set of skeleton diagrams for the self-energy up to second order, corresponding to the topologies (a)–(c). Since we conduct a self-consistent expansion in the dressed Green's function, we implicitly also sum any diagrams obtained by insertion of the topologies (a)–(c) into themselves, as exemplified by the diagrams (d),(e). Thus, in the self-consistent solution, the self-energy contains certain classes of diagrams up to infinite order. We do not include any diagrams corresponding to forward scattering, since these merely equate to a shift in the chemical potential, while we are interested in this problem at a specific stoichiometry where the node lies at the Fermi level.

starting guess for the self-energy given by

$$\Sigma^0(\mathbf{k}) = d_z^0 \sigma_z, \quad (16)$$

which in turn provides a corresponding Green's function $G^0(\omega, \mathbf{k})$. A stochastic summation of the expansion in V gives a new self-energy $\Sigma^1(\omega, \mathbf{k})$, which is subsequently used to construct the Green's function via Dyson's equation (13). This Green's function is then used to obtain a new self-energy $\Sigma^2(\omega, \mathbf{k})$, and so forth until convergence. The diagrams contributing to the self-energy are displayed in Figs. 2(a)–2(c). We sample these in the domain of momentum and imaginary time.

This scheme is repeated until relevant observables have converged. Near the phase transition, this typically requires several hundred iterations. We have used two starting configurations for the self-energy, featuring extremely small or relatively large symmetry-breaking terms, respectively. For most parameter regimes, these result in identical solutions.

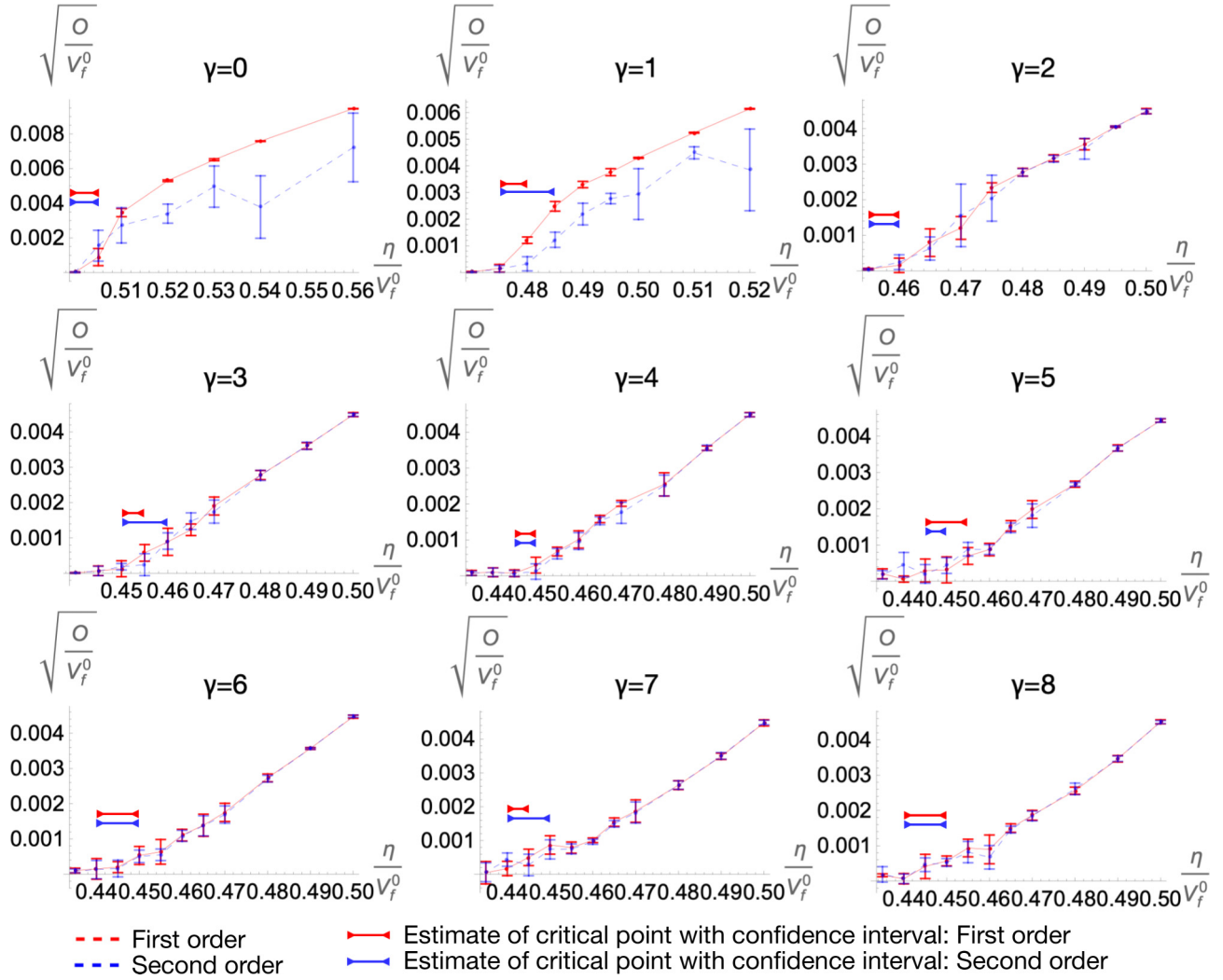


FIG. 3. The chiral order parameter O as a function of the interaction strength η in units of the bare Fermi velocity. The screening length is parametrized by $\lambda^{-1} = 10^{-2} \times 2^{-\gamma}$, while the inverse temperature is given by $\beta v_f^0 = 10^2 \times 2^\gamma$. Thus, the figures progress towards longer screening lengths and lower temperatures as γ increases. The red curves correspond to first order (self-consistent Fock theory), while the blue curves give the second-order self-consistent solution (see Fig. 2 for the included diagrams). Note that we display the square root of the order parameter since it is approximately quadratic in η over most parameter ranges. The colored bars indicate estimates for the critical point at first (red) and second order (blue) with confidence intervals. At the higher temperatures, the second-order expansion displays notable noise, but when the temperature decreases, these diagrams are suppressed by the vanishing density of states at the Fermi level.

However, at low temperatures and for a coupling strength that is slightly larger than the critical coupling, we observe a family of very fragile metastable symmetric solutions that likely result from competition between the symmetric and antisymmetric parts of the self-energy. The numerical value used for the published data is $d_z^0 = 10^3$, which ensures a large gap. To track the onset of a symmetry-broken phase, we define the chiral order parameter as follows. First, we note that the self-energy can be decomposed into frequency-independent and frequency-dependent parts, where the former stems from contributions that have a δ -function in imaginary time [like the Fock term in Fig. 2(a)]. The frequency-independent part of the self-energy can be written

$$\Sigma(\mathbf{k}) = \mathbf{d}(\mathbf{k}) \cdot \boldsymbol{\sigma}. \quad (17)$$

The chiral symmetry-breaking is generated by the z -component, prompting us to define an order parameter

of the form

$$O = \frac{1}{2\pi} \int d\mathbf{k} d_z(\mathbf{k}). \quad (18)$$

Thus, the order parameter is obtained from the σ_z -component of the frequency-independent part of $\Sigma(\mathbf{k})$. Since we consider a straight nodal line, we assume a solution that is translation-invariant in the z -direction. Furthermore, we assume a symmetry of the self-energy

$$e^{-i\phi\sigma_z/2} \Sigma(\omega, \mathbf{k}) e^{i\phi\sigma_z/2} = \Sigma(\omega, R_\phi^z \mathbf{k}), \quad (19)$$

where R_ϕ^z represents a rotation around the z -axis by ϕ .

The results from the simulations are summarized in Fig. 3. The dots represent raw data points at an expansion order of $N = 1$ and 2, respectively, while the lines are guides to the eye. For most parameter ranges, the order parameter scales approximately as $O \sim (\eta/v_f^0)^2$, prompting us to plot the square

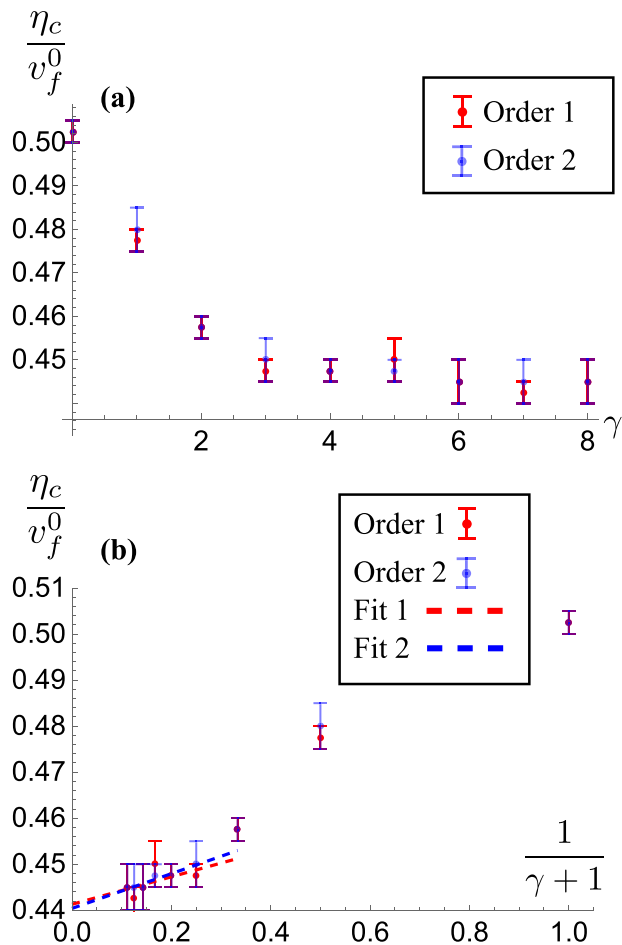


FIG. 4. Critical coupling strength (a) in units of the bare Fermi velocity v_f^0 for progressively lower temperatures and longer screening lengths, parametrized as $\lambda^{-1} = 10^{-2} \times 2^{-\gamma}$ and $\beta v_f^0 = 10^2 \times 2^\gamma$. For $\gamma \geq 3$ we estimate the critical coupling to $\eta_c/v_f^0 = 0.45 \pm 0.01$. The corrections at second order are not discernible at this accuracy. In (b) we plot the critical coupling strength against $(\gamma + 1)^{-1}$ and fit straight lines to the data points satisfying $\gamma \geq 4$. Extrapolating to $(\gamma + 1)^{-1} \rightarrow 0$ we find intersections with the y -axis at $\eta_c/v_f^0 = 0.441$ at first order and $\eta_c/v_f^0 = 0.440$ at second order, which falls within our confidence interval.

root. The solutions correspond to different values of γ , which controls the model parameters according to (15). The inserted boxes give estimates for the critical point where the order parameter approaches zero at first and second order.

Figure 4 gives a summary of the estimated coupling strength as a function of γ , extracted from Fig. 3. As the temperature is reduced and the screening length diverges, the critical coupling tends to saturate. For $\gamma \geq 3$, we find that the critical point is located at $\eta_c/v_f^0 = 0.45 \pm 0.01$. This corresponds to a screening length of $800 \leq \Lambda\gamma \leq 25\,600$.

The correction from first to second order falls within the error bars, suggesting that this problem may be well captured by self-consistent Fock theory. This is consistent with previous applications of diagrammatic techniques to semimetallic systems: In Weyl semimetals, the correction to the Green's function is almost entirely contained in the

frequency-independent part of the self-energy, leading to the emergence of virtually free fermions [33]. In graphene, at least the long-range part of the interaction drives the system towards an asymptotically free Dirac liquid [23], while for short-range interactions the convergence of the series has been demonstrated analytically up to a finite threshold [34].

The fact that semimetals with long-range interaction—in sharp contrast to metals—are dominated by Fock theory can be understood from their vanishing density of states at the Fermi level: In the absence of a Fermi surface, any diagram corresponding to excitation of the background is exponentially suppressed as $\sim \exp(-\beta\epsilon_k)$, meaning that it rapidly vanishes at low temperature [33]. Furthermore, the Fock term imposes a correction to the effective dispersion that scales as $\sim \alpha$. Therefore, even for an arbitrarily strong interaction, the effective expansion parameter is $\sim \alpha/\alpha$, which remains of order unity. It should also be stressed that the Coulomb interaction gives a divergent correction to the Fermi velocity in the low-temperature limit, further reducing the density of states.

It has been observed that metallic systems frequently feature divergencies of the diagrammatic series for strong interactions and at low temperature. When applying a bold diagrammatic scheme to a divergent series, this can result in false convergence to a fix-point that does not represent a physical solution [35,36]. This phenomenon has not been reported in any semimetals, where convergence of the series often persists in the low-temperature limit and for strong interaction. We attribute this to the vanishing density of states at the Fermi level and the simple structure of self-consistent Fock theory, which dominates the physics.

II. PHENOMENOLOGY OF THE SYMMETRY-BROKEN PHASE

In topological semimetals, central electronic properties are connected to the structure of the gap-closing points. Key examples of this include protected surface states [1,15] and novel magnetic responses like the chiral anomaly [37].

In the chiral phase, however, the gap-closing points are destroyed, meaning that some of these properties are either lost or substantially altered. Meanwhile, the presence of a macroscopic order parameter permits topological defects in the form of domain walls that interpolate between different chiralities. These defects introduce a new type of surface that can host localized states.

In this section, we explore how the chiral symmetry-breaking affects surface states and interferes with Landau levels, and we contrast these results with the symmetric regime. For this analysis we will adopt an effective model that captures the effect of symmetry-breaking on the dispersion:

$$H_{\text{eff}}(\mathbf{k}) = H_0(\mathbf{k}) + \Delta\sigma_z. \quad (20)$$

Here, $\Delta\sigma_z$ represents the effects of the chiral order.

A. Landau levels and magnetic response

To compute the Landau levels arising when the line-node is placed in a magnetic field, we consider a dispersion of the

form (1) and take the Fermi velocity to be unity. This gives

$$H_0(\mathbf{k}) = k_x \sigma_x + k_y \sigma_y = \begin{pmatrix} 0 & k_x - ik_y \\ k_x + ik_y & 0 \end{pmatrix}, \quad (21)$$

with energy bands

$$\varepsilon_{\pm} = \pm \sqrt{k_x^2 + k_y^2}. \quad (22)$$

Thus, the nodal line runs along the z -axis $(0, 0, k_z)$.

To couple the system to an external magnetic field, we introduce the displacement of the momentum \mathbf{k} by the vector potential \mathbf{A} :

$$\mathbf{k} \rightarrow \mathbf{k}' = \mathbf{k} + \mathbf{A}. \quad (23)$$

First, we consider a magnetic field along the z -direction, i.e., $\mathbf{B} = B\hat{z}$. Working in the axial gauge, the vector potential reads $\mathbf{A} = (-By/2, Bx/2, 0)$, so that we can define the ladder operators in terms of the new momenta,

$$a = \frac{k'_x - ik'_y}{\sqrt{2B}}, \quad a^\dagger = \frac{k'_x + ik'_y}{\sqrt{2B}}, \quad (24)$$

which allows us to write the Hamiltonian in the form

$$H_0 = \begin{pmatrix} 0 & \sqrt{2Ba} \\ \sqrt{2Ba}^\dagger & 0 \end{pmatrix}. \quad (25)$$

The Landau levels can be easily found from the eigenequation $H_0\Phi = E\Phi$. For $\Phi = (|\phi_1\rangle, |\phi_2\rangle)^T$, we obtain the two equations

$$\sqrt{2Ba}|\phi_2\rangle = E|\phi_1\rangle, \quad (26)$$

$$\sqrt{2Ba}^\dagger|\phi_1\rangle = E|\phi_2\rangle, \quad (27)$$

and, by inserting the first equation into the second, we arrive at

$$2Ba^\dagger a|\phi_2\rangle = E^2|\phi_2\rangle, \quad (28)$$

which describes a harmonic oscillator with

$$E = \pm\sqrt{2Bn}, \quad |\phi_2\rangle = c|n\rangle, \quad n = 0, 1, 2, \dots \in \mathbb{N}, \quad (29)$$

where c is a normalization constant. Then, for $|\phi_1\rangle$ we have

$$|\phi_1\rangle = \pm c|n-1\rangle. \quad (30)$$

Therefore, for a magnetic field in the z direction, the Landau levels are given by

$$E_{\pm} = \pm\sqrt{2Bn}, \quad (31)$$

with eigenstates

$$\Phi_{\pm} = c \begin{pmatrix} \pm|n-1\rangle \\ |n\rangle \end{pmatrix}. \quad (32)$$

The eigenstates appear as a spectrum of bands that are flat in all directions. The gap between these is controlled by the external field, as shown in Fig. 5. In contrast to Weyl semimetals, line-nodes do not give rise to a chiral anomaly [37] in the presence of a magnetic field. Instead, a single band remains at the Fermi level because the dispersion is independent of k_z .

For an in-plane field of the form $\mathbf{B} = B\hat{x}$, we may choose a vector potential of the form $\mathbf{A} = (0, -Bz/2, By/2)$. The

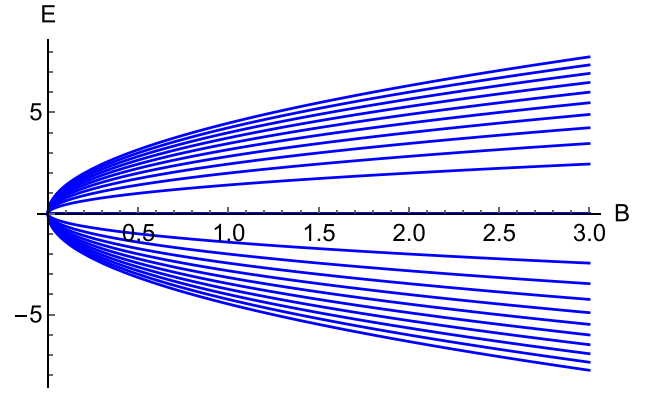


FIG. 5. Landau levels for the line-node semimetal in the presence of an external field $\mathbf{B} = B\hat{z}$, as a function of B as given by Eq. (31). Since the dispersion is independent of k_z , the energy levels are flat in all directions. A zero-energy mode remains for any value of the applied field.

ladder operators can then be constructed as

$$a = \frac{k'_y - ik'_z}{\sqrt{2B}}, \quad a^\dagger = \frac{k'_y + ik'_z}{\sqrt{2B}}. \quad (33)$$

Expressed in this language, the Hamiltonian (21) takes the form

$$H_0 = \begin{pmatrix} 0 & k_x - i\sqrt{\frac{B}{2}}(a + a^\dagger) \\ k_x + i\sqrt{\frac{B}{2}}(a + a^\dagger) & 0 \end{pmatrix}. \quad (34)$$

From the eigenequation $H_0\Phi = E\Phi$, we obtain for $|\phi_1\rangle$ and $|\phi_2\rangle$

$$\left[k_x - i\sqrt{\frac{B}{2}}(a + a^\dagger) \right] |\phi_2\rangle = E|\phi_1\rangle, \quad (35)$$

$$\left[k_x + i\sqrt{\frac{B}{2}}(a + a^\dagger) \right] |\phi_1\rangle = E|\phi_2\rangle. \quad (36)$$

As before, we can take the first equation and plug it into the second. By using the commutator $[a, a^\dagger] = 1$, we finally arrive at

$$\left[k_x^2 + \frac{B}{2}(a^2 + (a^\dagger)^2 + 2a^\dagger a + 1) \right] |\phi_2\rangle = E^2|\phi_2\rangle. \quad (37)$$

Solving Eq. (37) is complicated by the presence of terms of the form $\sim a^2$ and $\sim (a^\dagger)^2$, which render it anharmonic so that standard recipes for extracting the Landau levels are not applicable. For this reason, we adopt the Bargmann representation [38–40], which has been widely used in this scenario. Notably, this technique was applied to an anharmonic oscillator with a quartic potential [41] and the two-mode squeeze harmonic oscillator and the k th-order harmonic generation [42]. In this representation, the ladder operators are related to a complex variable z according to

$$a^\dagger = z, \quad a = \frac{d}{dz}, \quad (38)$$

while the wave function is a holomorphic function of z only, namely,

$$|\phi_1\rangle = \varphi_1(z), \quad |\phi_2\rangle = \varphi_2(z). \quad (39)$$

Expressed in this formalism, Eq. (37) takes the form

$$\frac{B}{2}\varphi_2'' + Bz\varphi_2' + \left[\frac{B}{2}(z^2 + 1) + k_x^2\right]\varphi_2 = E^2\varphi_2, \quad (40)$$

where we have used the notation $\varphi_2' = \frac{d\varphi_2}{dz}$ and $\varphi_2'' = \frac{d^2\varphi_2}{dz^2}$.

The different quantum states correspond to solutions of this equation for corresponding quantum numbers, such as polynomials of degree n . In principle, it is possible to extract a solution in the form of a power series in z , though this turns out to be highly inefficient. Thus, we instead introduce a reparametrization of $\varphi_2(z)$ given by

$$\varphi_2(z) = e^{-z^2/2} \psi_2(z). \quad (41)$$

The differential equation then takes the form

$$\psi_2'' + \omega^2 \psi_2 = 0 \quad \text{with} \quad \omega^2 = \frac{2}{B}(k_x^2 - E^2). \quad (42)$$

The trivial solution consisting of a combination of two exponentials does not correspond to the Landau levels, and the energy E still appears as an arbitrary constant. To extract the nontrivial solutions, we need to introduce a change of variables of the form

$$\rho = e^z \quad \Rightarrow \quad z = \ln \rho, \quad (43)$$

which finally transforms the equation for ψ_2 into

$$\rho^2 \frac{d^2\psi_2}{d\rho^2} + \rho \frac{d\psi_2}{d\rho} + \omega^2 \psi_2 = 0. \quad (44)$$

Now, we may find solutions of this equation as a polynomial in ρ of degree n by considering

$$\psi_2(\rho) = \sum_{i=0}^n f_i \rho^i. \quad (45)$$

Plugging this into the equation, we obtain an expression in terms of the coefficients of the expansion f_i ,

$$\omega^2 f_0 + (1 + \omega^2)f_1 \rho + \sum_{i=2}^n (i^2 + \omega^2)f_i \rho^i = 0. \quad (46)$$

Since our assumption of a polynomial of degree n implies $f_n \neq 0$, it trivially follows that $n^2 + \omega^2 = 0$, giving Landau levels with an energy

$$E_{\pm} = \pm \sqrt{\frac{1}{2}n^2 B + k_x^2}, \quad (47)$$

together with $f_i = 0, \forall i \neq n$. The function ψ_2 then reads

$$\psi_2(\rho) = c \rho^n \quad \Rightarrow \quad \psi_2(z) = c e^{nz}, \quad (48)$$

where c is a normalization constant. Returning to the original wave-function component φ_2 , we get

$$\varphi_2(z) = c e^{nz - z^2/2}. \quad (49)$$

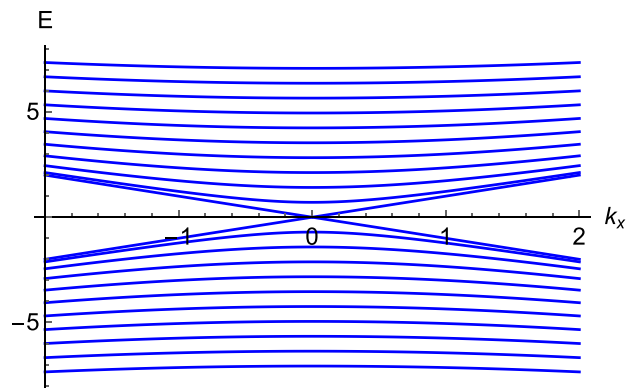


FIG. 6. Landau levels for the line-node semimetal in the presence of an external field $\mathbf{B} = \hat{x}$ ($B = 1$) as given by Eq. (47). In contrast to the case of a magnetic field along the \hat{z} direction in Fig. 5, the levels exhibit a momentum dependence. The two energy levels that are closest to the Fermi surface cross in the origin.

The φ_1 component may be written as

$$\varphi_{1,\pm}(z) = \frac{c}{E_{\pm}} \left(k_x - i\sqrt{\frac{B}{2}n} \right) e^{nz - z^2/2}. \quad (50)$$

In contrast to the Weyl semimetals, the states corresponding to $n = 0$ can be treated on an equal footing with the remaining levels. This quantum number gives two different states related by $E_1 = -E_2$ that cross the Fermi level at $k_x = 0$, as depicted in Fig. 6.

Finally, we will review these results once a symmetry-breaking term of the form $\Delta \sigma_z$ is included in the Hamiltonian. This gives

$$H_{\text{eff}}(\mathbf{k}) = k_x \sigma_x + k_y \sigma_y + \Delta \sigma_z = \begin{pmatrix} \Delta & k_x - ik_y \\ k_x + ik_y & -\Delta \end{pmatrix}. \quad (51)$$

Hence, the energy bands are now given by

$$\varepsilon_{\pm} = \pm \sqrt{k_x^2 + k_y^2 + \Delta^2}, \quad (52)$$

so that the system is an insulator. The symmetry-breaking perturbation introduced in the system has now gapped out the nodal line, suggesting that the Landau levels will form away from the Fermi level irrespective of the orientation of the magnetic field.

For the case of an external field $\mathbf{B} = B\hat{z}$ with ladder operators defined according to Eq. (24), the Hamiltonian reads

$$H_{\text{eff}} = \begin{pmatrix} \Delta & \sqrt{2Ba} \\ \sqrt{2Ba}^\dagger & -\Delta \end{pmatrix}. \quad (53)$$

Following the same approach as above and considering the eigenequation $H_{\text{eff}}\Phi = E\Phi$, we obtain a harmonic-oscillator-like equation for $|\phi_2\rangle$ with the solution

$$E_{\pm} = \pm \sqrt{2Bn + \Delta^2}, \quad |\phi_2\rangle = c |n\rangle, \quad (54)$$

where c is a normalization. Comparing with Eq. (31), we see that the effect of the perturbation Δ is to introduce a displacement of the Landau levels. On the other hand, for $|\phi_1\rangle$

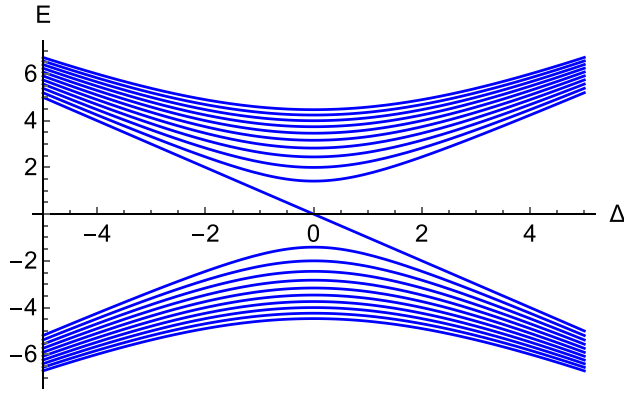


FIG. 7. Landau levels for a symmetry-broken line-node semimetal in the presence of an external field $\mathbf{B} = \hat{z}$ ($B = 1$) as a function of the symmetry-breaking parameter Δ . The applied field explicitly breaks the symmetry between the chiralities Δ and $-\Delta$, respectively, indicating that the chiral order can be manipulated via a magnetic field.

we have

$$|\phi_{1,\pm}\rangle = c \frac{\sqrt{2Bn}}{E_{\pm} - \Delta} |n-1\rangle. \quad (55)$$

This scenario is slightly different from the unperturbed case, and the value $n = 0$ needs to be considered separately since $|\phi_1\rangle = 0$ and $|\phi_2\rangle = |0\rangle$. As a result, the energy for $n = 0$ is given by $E_0 = -\Delta$. In conclusion, we thus find

$$E_0 = -\Delta, \quad E_{n,\pm} = \pm\sqrt{2Bn + \Delta^2}, \quad \forall n \neq 0. \quad (56)$$

Figure 7 shows the Landau levels (56) for $B = 1$ as a function of the symmetry-breaking parameter Δ . Besides the aforementioned displacement of the energy levels for $n \neq 0$, the unperturbed $E_0 = 0$ state is shifted relative to the Fermi level depending on Δ in a similar manner to the k_z -dependence of the Landau levels appearing in Weyl semimetals. Thus, for a symmetry-broken state, the magnetic field lifts the degeneracy between the two chiralities, implying that this degree of freedom can be manipulated by an external field in experiments.

Finally, we consider the case of an in-plane magnetic field $\mathbf{B} = B\hat{x}$ in the symmetry-broken phase. Expressed in the ladder operators defined in Eq. (33), the Hamiltonian takes the form

$$H_{\text{eff}} = \begin{pmatrix} \Delta & k_x - i\sqrt{\frac{B}{2}}(a + a^\dagger) \\ k_x + i\sqrt{\frac{B}{2}}(a + a^\dagger) & -\Delta \end{pmatrix}. \quad (57)$$

As before, the eigenvalue equation gives rise to an anharmonic problem, meaning that we have to rely on the Bargmann representation. For $|\phi_2\rangle$ the solution is given by Eq. (37), except for a shift in energy given by $E^2 \rightarrow E^2 - \Delta^2$. Hence, we can use the same protocol as above for the in-plane field with the ω parameter accordingly modified to

$$\omega^2 = \frac{2}{B}(k_x^2 - E^2 + \Delta^2). \quad (58)$$

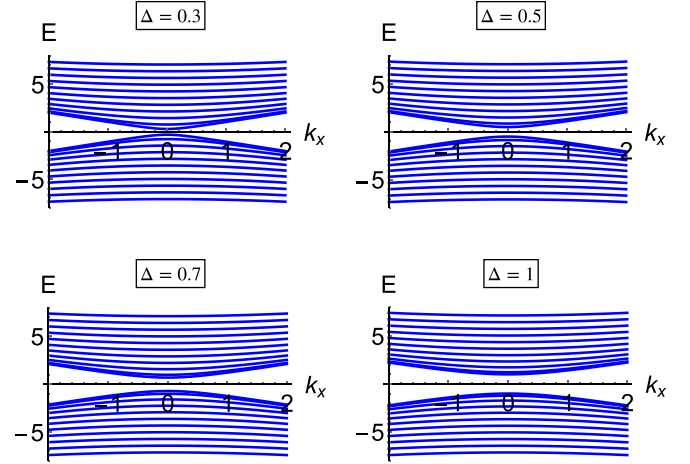


FIG. 8. Landau levels for the symmetry-broken line-node semimetal in the presence of an external field $\mathbf{B} = \hat{x}$ ($B = 1$). As the system becomes gapped, the crossing of the Landau levels shown in Fig. 6 is lifted.

The Landau levels are given by

$$E_{\pm} = \pm\sqrt{\frac{1}{2}n^2B + k_x^2 + \Delta^2}, \quad (59)$$

with the wave-function components

$$\phi_{1,\pm}(z) = \frac{c}{E_{\pm} - \Delta} \left(k_x - i\sqrt{\frac{B}{2}}n \right) e^{mz - z^2/2}, \quad (60)$$

$$\phi_2(z) = c e^{mz - z^2/2}, \quad (61)$$

where c is a normalization constant. In the symmetry-broken phase, the system becomes gapped, with Landau levels situated at finite energies, as seen in Fig. 8. The levels closest to the Fermi surface attain a gap of $|\Delta|$, which is thus independent of the chirality.

B. Interface states

In the symmetric phase, the line-node semimetals exhibit metallic drum-head surface states [15], which are generalizations of the Fermi arcs that occur in the Weyl semimetals [1]. These states are stabilized by a combination of topology and symmetry in the sense that the states are topologically protected in a subspace generated by the symmetry. Once this symmetry is spontaneously broken, the lines are gapped out, and the edge states are no longer protected.

However, the symmetry-broken phase permits domain walls that interpolate between regions of different chirality, on which the symmetry-breaking term Δ changes sign. This opens the possibility for metallic interface states that are bound to these topological defects. To model this scenario, we consider a domain wall described by

$$\Delta = \Delta(y) = \begin{cases} \Delta_+, & y > 0, \\ \Delta_-, & y < 0, \\ 0, & y = 0, \end{cases} \quad (62)$$

where $\Delta_+ > 0$ and $\Delta_- < 0$ are constants.

To identify the interface states, we apply an analytical approach based on trial functions that has been applied to Fermi

arcs within Weyl semimetals in semi-infinite systems [43,44]. Since $\Delta(y)$ is translation-invariant in the \hat{x} and \hat{z} directions but not along \hat{y} , it follows that k_x and k_z are good quantum numbers while k_y is not. Hence, we conduct the substitution $k_y \rightarrow -i\partial_y$, which transforms the effective Hamiltonian into

$$H_{\text{eff}}(k_x, -i\partial_y, k_z, y) = k_x\sigma_x - i\partial_y\sigma_y + \Delta(y)\sigma_z. \quad (63)$$

Next, we introduce a trial wave function of the form

$$\Psi(x, y, z) = \psi_\lambda |x, z\rangle = \begin{pmatrix} \psi_1 \\ \psi_2 \end{pmatrix} e^{\lambda y} |x, z\rangle. \quad (64)$$

Therefore, our problem is reduced to the eigenequation

$$H_{\text{eff}}(k_x, -i\partial_y, k_z, y)\Psi = E\Psi, \quad (65)$$

with a continuity condition at $\Psi(y=0)$. The secular equation, $\det|H(k_x, -i\partial_y, k_z, y) - E| = 0$, may be used to find the possible values of λ , namely

$$\lambda = \pm\sqrt{k_x^2 + \Delta^2 - E^2}. \quad (66)$$

Requiring the wave function to vanish at $y \rightarrow \pm\infty$, we need to separate the two regions of different chirality into Ψ_+ for $y > 0$ and Ψ_- for $y < 0$. Then, we obtain

$$\Psi_+ = c_+ \psi_{\lambda_+} |x, z\rangle = c_+ \begin{pmatrix} \psi_1^+ \\ \psi_2^+ \end{pmatrix} e^{\lambda_+ y} |x, z\rangle, \quad (67)$$

$$\Psi_- = c_- \psi_{\lambda_-} |x, z\rangle = c_- \begin{pmatrix} \psi_1^- \\ \psi_2^- \end{pmatrix} e^{\lambda_- y} |x, z\rangle, \quad (68)$$

where c_\pm are constants while

$$\lambda_\pm = \mp\sqrt{k_x^2 + \Delta_\pm^2 - E^2}. \quad (69)$$

On the other hand, for the eigenstates there are two possible sets of spinors $\psi^\pm = (\psi_1^\pm, \psi_2^\pm)^T$:

$$\psi^\pm = \begin{pmatrix} \lambda_\pm - k_x \\ \Delta_\pm - E \end{pmatrix} \quad \text{and} \quad \psi^\pm = \begin{pmatrix} \Delta_\pm + E \\ \lambda_\pm + k_x \end{pmatrix}. \quad (70)$$

Imposing that the solution is continuous at $y=0$, we obtain

$$c_+ \psi_{\lambda_+}(y=0, E) = c_- \psi_{\lambda_-}(y=0, E), \quad (71)$$

or equivalently,

$$c_+ \psi^+ - c_- \psi^- = 0. \quad (72)$$

Thus, the condition (72) gives us a system of two equations with two unknowns, c_+ and c_- . Hence, to have a nontrivial solution, it is necessary that

$$\det|\psi^+ - \psi^-| = 0. \quad (73)$$

Imposing this condition on the eigenvectors defined by Eq. (70) and using Eq. (62), we find

$$-(\lambda_+ - k_x)E + (\lambda_- - k_x)E = 0, \quad (74)$$

$$(\lambda_- + k_x)E - (\lambda_+ + k_x)E = 0, \quad (75)$$

which reduces to

$$\lambda_+ = \lambda_- = 0 \quad \Rightarrow \quad E = \pm k_x. \quad (76)$$

Therefore, we obtain two localized states proximate to the interface $y=0$ given by the wave functions

$$\Psi_\pm(E = -k_x) = c_\pm \begin{pmatrix} -\Delta_\pm - k_x \\ \Delta_\pm + k_x \end{pmatrix} e^{-\Delta_\pm y} |x, z\rangle, \quad (77)$$

$$\Psi_\pm(E = k_x) = c_\pm \begin{pmatrix} \Delta_\pm + k_x \\ -\Delta_\pm + k_x \end{pmatrix} e^{-\Delta_\pm y} |x, z\rangle, \quad (78)$$

where c_\pm is the normalization. At $k_x = 0$ these meet at the Fermi level, implying a metallic interface state in the form of a line-node that is exponentially localized to the domain wall.

To solve the problem of interface states on a domain wall for a more realistic gap Δ , which is continuous in y , it is generally necessary to apply numerical methods since the analytical technique introduced above cannot be applied when the gap has an explicit dependence on y . To obtain a numerically tractable problem in this scenario, we first conduct an inverse Fourier transform on y and consider a finite system that can be diagonalized to find the possible surface states. For this purpose, we consider a Hamiltonian that is periodic in k_y instead of its continuum equivalent:

$$H_0 = \sin k_x \sigma_x + \sin k_y \sigma_y. \quad (79)$$

Explicitly writing the creation and annihilation operators, we find

$$H_0 = \sum_{\mathbf{k}} [\sin k_x (a_{\mathbf{k}}^\dagger b_{\mathbf{k}} + b_{\mathbf{k}}^\dagger a_{\mathbf{k}}) + i \sin k_y (-a_{\mathbf{k}}^\dagger b_{\mathbf{k}} + b_{\mathbf{k}}^\dagger a_{\mathbf{k}})]. \quad (80)$$

The inverse Fourier transforms along the \hat{y} direction take the form

$$a_{\mathbf{k}} = \frac{1}{\sqrt{M}} \sum_j e^{-ik_y j} a_{\mathbf{k}_\parallel, j}, \quad b_{\mathbf{k}} = \frac{1}{\sqrt{M}} \sum_j e^{-ik_y j} b_{\mathbf{k}_\parallel, j}, \quad (81)$$

where M corresponds to the number of layers in the \hat{y} direction, j is the layer index, and \mathbf{k}_\parallel denotes the momentum parallel to the (010) surface. Thus, we obtain

$$H_0 = \sum_{\mathbf{k}_\parallel, j} \left[\sin k_x \mathbf{c}_{\mathbf{k}_\parallel, j}^\dagger \sigma_x \mathbf{c}_{\mathbf{k}_\parallel, j} - \frac{i}{2} \mathbf{c}_{\mathbf{k}_\parallel, j}^\dagger \sigma_y \mathbf{c}_{\mathbf{k}_\parallel, j+1} \right. \quad (82)$$

$$\left. + \frac{i}{2} \mathbf{c}_{\mathbf{k}_\parallel, j+1}^\dagger \sigma_y \mathbf{c}_{\mathbf{k}_\parallel, j} \right], \quad (83)$$

where we have defined

$$\mathbf{c}_{\mathbf{k}_\parallel, j} = (a_{\mathbf{k}_\parallel, j}, b_{\mathbf{k}_\parallel, j})^T. \quad (84)$$

In this case, the symmetry-breaking contribution to the full Hamiltonian may be written as

$$H_\Delta = \sum_{\mathbf{k}_\parallel, j} \Delta(j) \mathbf{c}_{\mathbf{k}_\parallel, j}^\dagger \sigma_z \mathbf{c}_{\mathbf{k}_\parallel, j}, \quad (85)$$

where the dependence on y is translated into the layer labeled j . As before, we are interested in a perturbation $\Delta(j)$ that changes sign at $y=0$. We consider the scenarios of both an even or odd number of layers. In the latter case, we take $j_0 = \frac{1}{2}(M+1)$ so that the middle layer j_0 corresponds to $y=0$, implying that Δ vanishes at $y=0$. We consider a linear

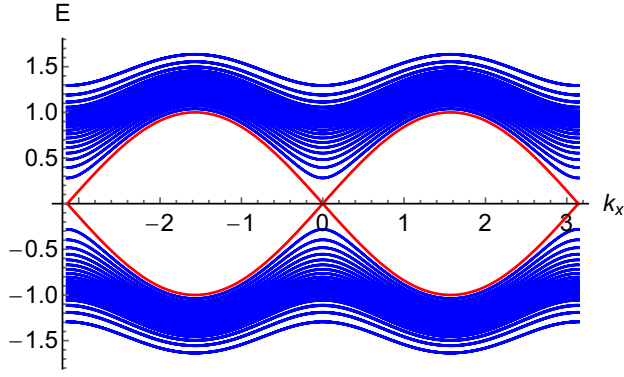


FIG. 9. Metallic interface states situated at a domain wall that interpolates between different signs on the chiral order parameter. The energy levels correspond to a system with 51 layers in the \hat{y} -direction with a linear symmetry-breaking term given by Eq. (86). The red lines correspond to a family of solutions that are exponentially localized to the middle layer that exhibits a line node at $k_x = 0$.

perturbation ranging from $-\Delta_0$ to $+\Delta_0$, with $\Delta_0 > 0$, that is given by

$$\Delta(j) = 2 \frac{j-1}{M-1} \Delta_0 - \Delta_0. \quad (86)$$

For an even number of layers, the gap function Δ given by (86) does not vanish anywhere since there is no center layer. In Fig. 9 we display the corresponding energy dispersion for the different states with $\Delta_0 = 1$ and a total number of layers $M = 51$ as a function of k_x (note that the solution is independent of k_z). The states plotted in red exhibit a gap-closing point at $k_x = n\pi$, implying that a line node is present. To establish the spatial extent of the nodal states, we introduce the following metric:

$$\Pi(j) = \frac{|\psi_j|^2}{\Psi^\dagger \Psi}, \quad (87)$$

where $\Psi = (\psi_1, \psi_2, \dots, \psi_j, \dots, \psi_M)^T$ is the wave function of the state. The metric (87) is shown in Fig. 10, revealing that the metallic interface state is exponentially localized to the center layer j_0 .

One may note that, after the introduction of $\Delta(j)$, the system is gapped in every layer but the one corresponding to j_0 , where $\Delta(j_0) = 0$. It should therefore be expected that the interface states fall off as

$$\frac{1}{c_0} e^{-\Delta(j)(j-j_0)}, \quad (88)$$

where c_0 is a normalization constant. The red curve in Fig. 10 shows a fit of the form (88) with c_0 as a free parameter, revealing that there is an excellent agreement. The result for an even number of layers was found to be indistinguishable from the case of an odd number implying that the metallic interface states do not depend on details of the domain wall.

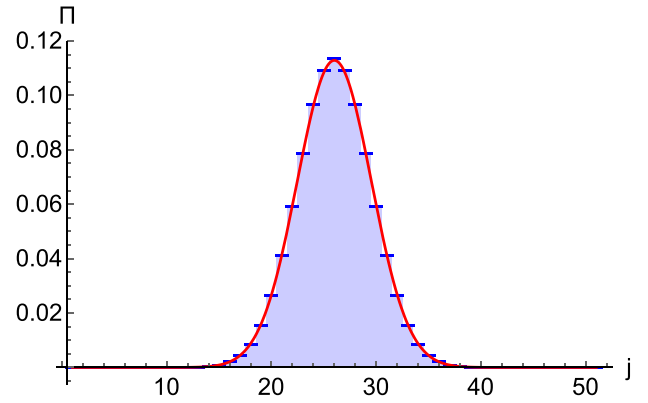


FIG. 10. Exponentially localized interface states. The blue curve presents the spatial extent of the localized states as defined by the metric (87). The red curve represents a fit of the form (88), displaying excellent agreement.

III. SUMMARY

We have examined the stability of line-node semimetals in the presence of Coulomb interactions and found a chiral instability occurring at a finite interaction strength. The chiral order parameter exhibits a well-defined behavior in the limit of an infinite screening length, despite the presence of infrared divergencies in this problem.

By computing the Landau levels, we observe that an out-of-plane magnetic field couples to the chiral order parameter, thus lifting the degeneracy of the two ground states. This provides the means to select a specific chirality in experiments.

The spontaneous breaking of a Z_2 symmetry allows for the creation of topological defects in the form of domain walls that interpolate between the two ground states. We observe that these walls are associated with metallic interface states in the otherwise insulating system. We also note that the drum-head surface states that exist in the symmetric regime are gapped out in the chiral phase.

By the application of magnetic fields which couple to the chiral order, we expect that it becomes possible to create domain walls in experiments. If a domain wall is created in a system with a concave geometry, then it can be trapped on a “bottleneck,” since the energy cost is proportional to its area [45]. This would allow observation of the domain wall without an applied field.

ACKNOWLEDGMENTS

This work was supported by the Swedish Research Council (VR) through Grant No. 2018-03882 and Stiftelsen Olle Engkvist via Grant No. 204-0185. Computations were performed on resources provided by the Swedish National Infrastructure for Computing (SNIC) at the National Supercomputer Centre in Linköping, Sweden. J.C. would like to thank Lars Fritz for important input and discussions.

- [1] S. Jia, S.-Y. Xu, and M. Z. Hasan, Weyl semimetals, fermi arcs and chiral anomalies, *Nat. Mater.* **15**, 1140 (2016).
- [2] A.-Q. Wang, X.-G. Ye, D.-P. Yu, and Z.-M. Liao, Topological semimetal nanostructures: From properties to topotronics, *ACS Nano* **14**, 3755 (2020).
- [3] J. Ma, Q. Gu, Y. Liu, J. Lai, P. Yu, X. Zhuo, Z. Liu, J.-H. Chen, J. Feng, and D. Sun, Nonlinear photoresponse of type-ii weyl semimetals, *Nat. Mater.* **18**, 476 (2019).
- [4] W. Han, Y. C. Otani, and S. Maekawa, Quantum materials for spin and charge conversion, *npj Quantum Mater.* **3**, 27 (2018).
- [5] N. Kumar, Y. Sun, N. Xu, K. Manna, M. Yao, V. Süss, I. Leermakers, O. Young, T. Förster, M. Schmidt, H. Borrmann, B. Yan, U. Zeitler, M. Shi, C. Felser, and C. Shekhar, Extremely high magnetoresistance and conductivity in the type-ii weyl semimetals WP_2 and MoP_2 , *Nat. Commun.* **8**, 1642 (2017).
- [6] Y. Wang, E. Liu, H. Liu, Y. Pan, L. Zhang, J. Zeng, Y. Fu, M. Wang, K. Xu, Z. Huang, Z. Wang, H.-Z. Lu, D. Xing, B. Wang, X. Wan, and F. Miao, Gate-tunable negative longitudinal magnetoresistance in the predicted type-ii weyl semimetal WTe_2 , *Nat. Commun.* **7**, 13142 (2016).
- [7] Y. Sun, Y. Zhang, C. Felser, and B. Yan, Strong Intrinsic Spin Hall Effect in the TaAs Family of Weyl Semimetals, *Phys. Rev. Lett.* **117**, 146403 (2016).
- [8] B. Singh, G. Chang, T.-R. Chang, S.-M. Huang, C. Su, M.-C. Lin, H. Lin, and A. Bansil, Tunable double-weyl fermion semimetal state in the $SrSi_2$ materials class, *Sci. Rep.* **8**, 10540 (2018).
- [9] C. Fang, M. J. Gilbert, X. Dai, and B. A. Bernevig, Multi-Weyl Topological Semimetals Stabilized by Point Group Symmetry, *Phys. Rev. Lett.* **108**, 266802 (2012).
- [10] B. Bradlyn, J. Cano, Z. Wang, M. G. Vergniory, C. Felser, R. J. Cava, and B. A. Bernevig, Beyond dirac and weyl fermions: Unconventional quasiparticles in conventional crystals, *Science* **353**, aaf5037 (2016).
- [11] P. Tang, Q. Zhou, and S.-C. Zhang, Multiple Types of Topological Fermions in Transition Metal Silicides, *Phys. Rev. Lett.* **119**, 206402 (2017).
- [12] T. Bzdušek, Q. Wu, A. Rüegg, M. Sigrist, and A. A. Soluyanov, Nodal-chain metals, *Nature (London)* **538**, 75 (2016).
- [13] T. Bzdušek and M. Sigrist, Robust doubly charged nodal lines and nodal surfaces in centrosymmetric systems, *Phys. Rev. B* **96**, 155105 (2017).
- [14] G. Bian, T.-R. Chang, R. Sankar, S.-Y. Xu, H. Zheng, T. Neupert, C.-K. Chiu, S.-M. Huang, G. Chang, I. Belopolski, D. S. Sanchez, M. Neupane, N. Alidoust, C. Liu, B. Wang, C.-C. Lee, H.-T. Jeng, C. Zhang, Z. Yuan, S. Jia *et al.*, Topological nodal-line fermions in spin-orbit metal $PbTaSe_2$, *Nat. Commun.* **7**, 10556 (2016).
- [15] G. Bian, T.-R. Chang, H. Zheng, S. Velury, S.-Y. Xu, T. Neupert, C.-K. Chiu, S.-M. Huang, D. S. Sanchez, I. Belopolski, N. Alidoust, P.-J. Chen, G. Chang, A. Bansil, H.-T. Jeng, H. Lin, and M. Z. Hasan, Drumhead surface states and topological nodal-line fermions in $ltase_2$, *Phys. Rev. B* **93**, 121113(R) (2016).
- [16] A. Yamakage, Y. Yamakawa, Y. Tanaka, and Y. Okamoto, Line-node dirac semimetal and topological insulating phase in noncentrosymmetric pnictides $CaGx$ ($x = p, as$), *J. Phys. Soc. Jpn.* **85**, 013708 (2016).
- [17] L. S. Xie, L. M. Schoop, E. M. Seibel, Q. D. Gibson, W. Xie, and R. J. Cava, A new form of Ca_3P_2 with a ring of dirac nodes, *APL Mater.* **3**, 083602 (2015).
- [18] S. Kobayashi, Y. Yamakawa, A. Yamakage, T. Inohara, Y. Okamoto, and Y. Tanaka, Crossing-line-node semimetals: General theory and application to rare-earth trihydrides, *Phys. Rev. B* **95**, 245208 (2017).
- [19] O. Vafek and K. Yang, Many-body instability of coulomb interacting bilayer graphene: Renormalization group approach, *Phys. Rev. B* **81**, 041401(R) (2010).
- [20] B. Roy, P. Goswami, and V. Juričić, Interacting weyl fermions: Phases, phase transitions, and global phase diagram, *Phys. Rev. B* **95**, 201102(R) (2017).
- [21] B. Roy, Interacting nodal-line semimetal: Proximity effect and spontaneous symmetry breaking, *Phys. Rev. B* **96**, 041113(R) (2017).
- [22] M. V. Ulybyshev, P. V. Buividovich, M. I. Katsnelson, and M. I. Polikarpov, Monte Carlo Study of the Semimetal-Insulator Phase Transition in Monolayer Graphene with a Realistic Interelectron Interaction Potential, *Phys. Rev. Lett.* **111**, 056801 (2013).
- [23] I. S. Tupitsyn and N. V. Prokof'ev, Stability of Dirac Liquids with Strong Coulomb Interaction, *Phys. Rev. Lett.* **118**, 026403 (2017).
- [24] L. M. Schoop, M. N. Ali, C. Straßer, A. Topp, A. Varykhalov, D. Marchenko, V. Duppl, S. S. P. Parkin, B. V. Lotsch, and C. R. Ast, Dirac cone protected by non-symmorphic symmetry and three-dimensional dirac line node in $zrsis$, *Nat. Commun.* **7**, 11696 (2016).
- [25] Y. Shao, A. N. Rudenko, J. Hu, Z. Sun, Y. Zhu, S. Moon, A. J. Millis, S. Yuan, A. I. Lichtenstein, D. Smirnov, Z. Q. Mao, M. I. Katsnelson, and D. N. Basov, Electronic correlations in nodal-line semimetals, *Nat. Phys.* **16**, 636 (2020).
- [26] K. Van Houcke, E. Kozik, N. Prokof'ev, and B. Svistunov, Diagrammatic monte carlo, *Phys. Proc.* **6**, 95 (2010).
- [27] J. Carlström and E. J. Bergholtz, Symmetry-enforced stability of interacting weyl and dirac semimetals, *Phys. Rev. B* **97**, 161102(R) (2018).
- [28] R. Rossi, Determinant Diagrammatic Monte Carlo Algorithm in the Thermodynamic Limit, *Phys. Rev. Lett.* **119**, 045701 (2017).
- [29] R. Rossi, N. Prokof'ev, B. Svistunov, K. Van Houcke, and F. Werner, Polynomial complexity despite the fermionic sign, *Europhys. Lett.* **118**, 10004 (2017).
- [30] J. Carlström, Strong-coupling diagrammatic monte carlo technique for correlated fermions and frustrated spins, *Phys. Rev. B* **103**, 195147 (2021).
- [31] A. L. Fetter and J. D. Walecka, *Quantum Theory of Many-particle Systems* (Dover, Mineola, New York, 1971).
- [32] J. Carlström, Diagrammatic monte carlo procedure for the spin-charge transformed hubbard model, *Phys. Rev. B* **97**, 075119 (2018).
- [33] J. Carlström and E. J. Bergholtz, Strongly interacting weyl semimetals: Stability of the semimetallic phase and emergence of almost free fermions, *Phys. Rev. B* **98**, 241102(R) (2018).
- [34] A. Giuliani and V. Mastropietro, Rigorous construction of ground state correlations in graphene: Renormalization of the velocities and ward identities, *Phys. Rev. B* **79**, 201403(R) (2009).

- [35] E. Kozik, M. Ferrero, and A. Georges, Nonexistence of the Luttinger-Ward Functional and Misleading Convergence of Skeleton Diagrammatic Series for Hubbard-Like Models, *Phys. Rev. Lett.* **114**, 156402 (2015).
- [36] O. Gunnarsson, G. Rohringer, T. Schäfer, G. Sangiovanni, and A. Toschi, Breakdown of Traditional Many-Body Theories for Correlated Electrons, *Phys. Rev. Lett.* **119**, 056402 (2017).
- [37] N. P. Armitage, E. J. Mele, and A. Vishwanath, Weyl and dirac semimetals in three-dimensional solids, *Rev. Mod. Phys.* **90**, 015001 (2018).
- [38] V. Bargmann, On the representations of the rotation group, *Rev. Mod. Phys.* **34**, 829 (1962).
- [39] V. Bargmann, On a hilbert space of analytic functions and an associated integral transform. part i, *Commun. Pure Appl. Math.* **14**, 187 (1961).
- [40] V. Bargmann, On a hilbert space of analytic functions and an associated integral transform. part ii, *Commun. Pure Appl. Math.* **20**, 1 (1967).
- [41] F. T. Hioe and E. W. Montroll, Quantum theory of anharmonic oscillators. i. energy levels of oscillators with positive quartic anharmonicity, *J. Math. Phys.* **16**, 1945 (1975).
- [42] Y.-Z. Zhang, Solving the two-mode squeezed harmonic oscillator and the k th-order harmonic generation in bargmann-hilbert spaces, *J. Phys. A* **46**, 455302 (2013).
- [43] S.-B. Zhang, H.-Z. Lu, and S.-Q. Shen, Linear magnetoconductivity in an intrinsic topological weyl semimetal, *New J. Phys.* **18**, 053039 (2016).
- [44] T. Ojanen, Helical fermi arcs and surface states in time-reversal invariant weyl semimetals, *Phys. Rev. B* **87**, 245112 (2013).
- [45] J. Garaud and E. Babaev, Domain Walls and Their Experimental Signatures in $s + is$ Superconductors, *Phys. Rev. Lett.* **112**, 017003 (2014).